Molecular Therapy
Nucleic Acids
Original Article

Binding characterization of anthraquinone derivatives by stabilizing G-quadruplex DNA leads to an anticancerous activity

Arpita Dey,[1] Kumud Pandav,[1] Mala Nath,[2] Ritu Barthwal,[1] and Ramasare Prasad[1]

[1]Department of Biosciences and Bioengineering, Indian Institute of Technology Roorkee, Roorkee, Uttarakhand 247667, India; [2]Department of Chemistry, Indian Institute of Technology Roorkee, Roorkee, Uttarakhand 247667, India

G-quadruplex is a non-canonical secondary structure identified in the telomeric region and the promoter of many oncogenes. Anthraquinone derivatives, a well-known inducer of telomere disruption in malignant cells and activate the apoptotic pathway. We used biophysical and biochemical studies to confirm the interaction of synthesized anthraquinone derivatives with the human telomeric G-quadruplex sequence. The binding affinity of N-2DEA and N-1DEA are $K_b = 4.8 \times 10^6$ M^{-1} and $K_b = 7.6 \times 10^5$ M^{-1}, respectively, leading to hypochroism, fluorescence quenching with minor redshift and ellipticity variations indicating ligand binding in the external groove. We found that sodium ions induced stabilization more rather than potassium ions. Molecular docking of complex demonstrates a molecule's exterior binding to a quadruplex. The investigation of ROS activity indicated that the cell initiates mortality in response to the IC_{50} concentration. Cellular morphology, nuclear condensation, and fragmentation were altered in the treated cell, impairing cellular function. Finally, the transcriptional regulatory study paves the way for drug design as an anticancer agent because of the tremendous possibilities of changing substituent groups on anthraquinones to improve efficacy and selectivity for G-quartet DNA. Our research focused on how ligand binding to telomere sequences induces oxidative stress and inhibits the growth of malignant cells.

INTRODUCTION

According to non-covalent supermolecular bonding, such as the hydrogen bond Hoogsteen pattern in the presence of monovalent cation, the guanine-rich tandem repeat sequence in the complete genome can form G-quadruplex (G4) structures.[1] The G4 structure in the telomeric region prevents the access of telomerase enzyme from causing apoptosis and consequent cell death.[2] Depending on the length of the G rich sequences, loop length/size, and glycosidic bond in the presence of metal ions, G-quadruplex DNA structures take on several topologies, such as anti-parallel, parallel, and hybrid structures.[3,4] An individual strand of G-quadruplexes is constructed the Hoogsteen hydrogen bonding strategy to cyclically assemble four guanine bases in a square planar pattern.[5] The G-quartet structure provides a unique electron-rich aromatic surface consisting of four guanine bases for recognition and ligand binding because of its planar orientation. Quadruplex structures also have unique binding pockets, such as four independent groove areas with varied dimensions, which are identical in width in tetramolecular forms but have different widths in unimolecular forms. According to a previous study, in the presence of K^+/Na^+ solution, free wild-type 26-mer DNA (wHTel-26) and 22-mer telomere DNA(HTel-22) sequence form hybrid and antiparallal type G-quadruplex structures.[6,7] In 80%–85% of human cancers, telomerase is an inverse transcriptase activated to maintain telomeres.[8,9] The stabilization of the G-quadruplex DNA structures found in the human genome, for instance, in the promoting region of some oncogenes, as well as in telomeric 3′ overhangs that consist of tandem repeat of the G rich sequence, can regulate various cellular activities, such as replication, transcription, translation, telomerase association to the telomere.[10] The promoter regions of several proto-oncogenes, such as *c-MYC*,[11] *c-KIT*,[12] *c-MYB*, *BCL-2*[13] and *k-RAS*,[14] *VEGF*,[15] and immunoglobulin switch regions have high trend of G-rich sequences.[16]

According to reports, small compounds may also help stabilize G-quadruplex DNA conformation by downregulating protein expressions and suppressing cellular processes that lead to cell death.[17] Small compounds with long side chains designed to interact with the G-tetrad can be easily incorporated into the groove containing phosphate backbone to achieve adequate selectivity for quadruple binding to duplex DNA in a general method.[18–20] All anthraquinone-based anti-cancer agent exhibits the DNA binding property, for example, mitoxantrone.[21]

Anthraquinone compounds have also been shown to have anti-inflammatory, antiarthritis, antiviral, antibacterial, and possibly antimalarial and anti-multiple sclerosis properties.[22] One of the primary

Received 11 June 2022; accepted 11 November 2022;
https://doi.org/10.1016/j.omtn.2022.11.008.

Correspondence: Ritu Barthwal, PhD, Department of Biosciences and Bioengineering, Indian Institute of Technology Roorkee, Roorkee, Uttarakhand 247667, India.
E-mail: ritu.barthwal@bt.iitr.ac.in
Correspondence: Ramasare Prasad, PhD, Department of Biosciences and Bioengineering, Indian Institute of Technology Roorkee, Roorkee, Uttarakhand 247667, India.
E-mail: ramasare.prasad@bt.iitr.ac.in

obstacles in the design of G-quadruplex anti-cancer mediated drug is the selectivity of linking G-quadruplex to duplex DNA.[23] The first discovered 2, 6-disubstituted aminoalkyl amido anthraquinone show an affinity for G-quadruplex and inhibits telomerase at 23 μM and $\Delta T_m \sim 20°C$.[19] In peptidyl-anthraquinones, adding a hydrophobic residue (Phe) to the Lys residue at the 2, 6, or 2, 7 locations results in more excellent selectivity for G-quadruplex over duplex DNA and decreased toxicity.[20] Then, the amido-anthraquinone derivatives dislocated at various substituent locations with multiple lengths of a side chain are further advanced to obtain binding selectivity to G-quadruplex DNA.[24] Anthraquinone derivatives garnered substantial attention Because of their large <pi>-surface, which proficiently processes π-π interaction with G-tetrads.[25] Porphyrin, a well-known G quadruplex stabilizer, triggers the photosensitizer pathway, resulting in enhanced reactive oxygen species (ROS) production in cancer cells.[26] The piperidine anthraquinone derivative suppressed telomerase activity in Barrett's stomach cancer. Because of ubiquitin-conjugated c-*MYC* transcription factor proteolysis, inhibition has been associated with lower h-TERT telomerase reverse transcriptase enzyme levels and c-*MYC* transcription factor levels. There have been no significant structural investigations on this vital anti-tumor treatment, which employs quadruplex structures. This is why the binding mechanism, multi-spectroscopic investigation of DNA quadruplex structure, and anthraquinone derivatives are crucial.

The purpose of this study is to determine the effect of the length of the side chains of anthraquinone derivatives containing diethyl groups (changing N = CH_2 groups) on binding with G-quadruplexes under the influence of Na^+ and K^+ ions. Several biochemical and biophysical approaches were performed to evaluate the structural changes and thermal stability of the ligand-DNA after G4 ligand binding in the presence of K^+- and Na^+-rich solutions. Both ligands bind to telomeres or oncogene promoters, which induce oxidative stress and senescence, leading to anti-cancer activity in MCF-7 cell line investigations.

RESULTS

Real-time binding of two derivatives to the human telomere 22-mer G-quadruplex sequence

Structure-based drug design is perplexing because of the non-specific interaction of ligand and targeted sequence. As a result, ligand binding to the intended target is essential. Sensograms of N-1DEA and N-2DEA (Figures 1A and 1B) reveal that the steady-state reaction on binding to immobilized d-[AGGG(TTAGGG)$_3$] in K^+-rich solution increases with increasing concentration in the range of 0.03–5 M. At 25°C, the affinity kinetics of association and dissociation constants for N-2DEA and N-1DEA are $K_b = 4.8 \times 10^6\ M^{-1}$ and $K_b = 7.6 \times 10^5\ M^{-1}$, respectively. Both ligand affinity constants were calculated to be $K_b = 6.6 \times 10^5\ M^{-1}$ and $K_b = 3.0 \times 10^5\ M^{-1}$, respectively (Figures 1C and 1D). The one order higher in response to the binding constant of kinetics data shown for N-2DEA is more efficient than N-1DEA. Real-time binding experiment shows enhancement in steady-state response with increasing concentration demonstrates a specific interaction between two molecules. The more efficient binding nature shown in the case of N-2DEA is most probably more specific binding because of two CH_2 groups present in N-2DEA. The steady-state response indicated that more than one stoichiometry exists in a lower concentration of drug-DNA assembly.

Inducing absorption/emission changes after binding of anthraquinone derivatives to G-quadruplex structure

To assess the contribution of different ions, we examined the changes in absorption spectra upon binding of ligand to the G quartet. The absorption maxima of N-1DEA and N-2DEA are appeared at four distinct wavelengths: 224, 279, 303, and 352 nm. Stepwise addition of wHTel-26 DNA to N-1DEA has been observed in the visible region (at 352 nm approx) because absorbance of DNA extensively in the UV region resulting in redshift $\Delta\lambda_{max} \sim 6$ nm at D/N = 0.5 (Figure 2A). After adding HTel-22 DNA to N-1DEA, a redshift $\Delta\lambda_{max} \sim 8$ nm at D/N = 0.5 change in absorbance was observed (Figure 2C). A hypochromic impact of up to ∼27% was observed following the first addition of wHTel-26 DNA to N-1DEA, followed by an increase in absorbance after D/N = 2.5 (Figure 2A). At D/N = 0.5, hypochromic prevail up to ∼5.1%. However, when HTel-22 DNA is added, the hypochromic effect increases by 15%, followed by an increase in absorbance at D/N = 3.8, and hypochromicity persists for about 7% at D/N = 0.5 (Figure 2C). Correspondingly, the reciprocal of absorbance 1/A, as a function of D/N (Figures S1B and S1C) likewise displays an inflection point at D/N = 1.0 and 4.0 for wHTel-26, respectively, and D/N = 0.5 and 2.1 for HTel-22 DNA, indicating that the drug-DNA complex stoichiometry. The scattering of the data may be attributed to non-specific binding of the ligand to DNA. Changes in the absorbance may be attributed to the closeness of ligands with guanines where the electron transfer is favored and culminating strong bonds between two molecules are formed.[21]

In the case of N-2DEA, a significant shift was detected in the visible region after the stepwise addition of wHTel-26 DNA, culminating in a redshift of $\Delta\lambda_{max} \sim 6$ nm (Figure 2B) at D/N = 0.5; however, no shift was found in the case of HTel-22 DNA titration (Figure 2D). Following the first addition of wHTel-26 DNA to N-2DEA, a hypochromic effect of up to 21% was observed by an increase in absorbance after D/N = 2.5 (Figure 2B). Hypochroism obtains up to 19% at D/N = 0.5. However, in Figure 2D observed hypochromic effect is 11% at D/N = 0.5. Titration of N-2DEA with wHTel-26 and HTel-22 resulted in a 63% hypochromicity (Figure 2B) accompanied by a $\Delta\lambda_{max} \sim 5$ nm redshift. As a function of D/N, 1/A (Reciprocal of absorbance) reveals a shift in slope for wHTel-26 at D/N = 2.0 and 3.8 and HTel-22 at D/N = 1.0 and 2.0, respectively (Figures S2A and S2C). The intrinsic binding constants (Figures S2B and S2D) were calculated using a standard equation. As data did not fit into the combination of straight lines, Scatchard plots could not be used.[21,27–29] The appropriate binding constant was estimated using the Scatchard equation as described with the equation used in a previous study.[30]

The hyperchromicity followed by initial hypochromic with a strong redshift indicates the presence of at least two separate binding modes. Cyanine dye and TMPyP4 binding to parallel G-quadruplexes have previously been reported to show multiple binding sites, resulting in the absence of a definite isobestic point.[31,32] Notably, the existence

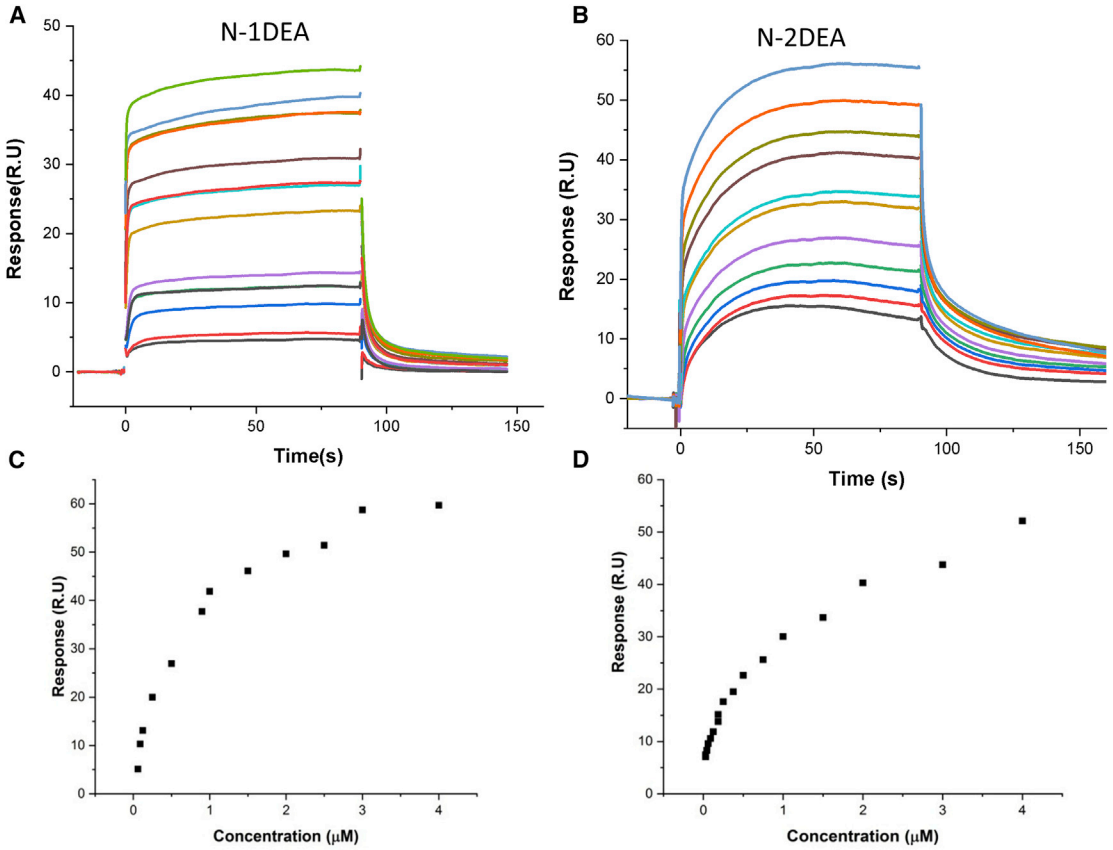

Figure 1. SPR sensograms for N-1DEA and N-2DEA demonstrating interaction with d-[AGGG(TTAGGG)$_3$]

SPR sensograms for (A) N-1DEA and (B) N-2DEA with increasing concentrations from 0.03 (bottom) to 5.0 (top) μM in HEPES buffer containing 100 mM KCl (pH 7.0), demonstrating interaction with d-[AGGG(TTAGGG)$_3$] at 25°C. Response of steady-state (R.U.) as a function of concentration of (C) N-1DEA and (D) N-2DEA with above concentrations.

of more than one binding sites has been reported on ligand binding to 22-mer and 21-mer human telomere DNA with approximately equivalent K_b values, resulting in 17% and 27% hypochromism, respectively, whereas we observed a similar hypochromic impact.[33,34] Classical intercalation mode of binding in duplex DNA causes a redshift of 20–45 nm; partial stacking of the quadruplex DNA induces an approximately Δ_{max} = 15 nm redshift. If an 8 nm redshift accompanies a significant hypochromic, exclude classical intercalation.[35] The evidence suggests that DNA is bound outwardly.

With increasing concentrations of wHTel-26 and HTel-22 DNA added to N-1DEA ligand, in fluorescence intensity, significant quenching was observed, which was 66% and 63% at D/N = 0.5, respectively, with a redshift of 6–10 nm at λ_{em} = 550 nm (Figures 3A and 3C). Similarly, with the consecutive additions of wHTel-26 and HTel-22 DNA to N-2DEA molecules (Figures 3B and 3D), 94% and 96% quenching in fluorescence intensity was observed at D/N = 0.5 (Figures 3B and 3D). At D/N = 4.0, quenching of fluorescence by N-1DEA drug results in a redshift of ∼10 nm (from 533 to 543 nm). Plotting fluorescence (F) of N-1DEA at 539 nm as a function of wHTel-26 concentration, [DNA], revealed a slope change at [DNA] = 1.75 and 4.0 μM (Figure S3A), which conform to D/N = 1.8 and 4.0, respectively, and reciprocal fluorescence (1/F), as a function of D/N (Figure S3B) revealed points of inflection at D/N = 1.0, 2.2, and 4.0, implying that stoichiometry might be indicating stoichiometry 1:1, 2:1, and 4:1. In the presence of sodium ions plotting fluorescence (F) of N-1DEA at 539 nm as a function of HTel-22 DNA concentration, [DNA] revealed a slope change at [DNA] = 1.7 and 3.5 μM (Figure S4A), which corresponds to D/N = 2.0 and 4.0, respectively, and reciprocal fluorescence, 1/F, as a function of D/N (Figure S4B), demonstrate the point of inflection at D/N = 1.0.

Plotting N-2DEA fluorescence (F) as a function of HTel-22 concentration, [DNA], revealed a change in slope at [DNA] = 1.0, 2.0, and 3.5 μM (Figure S6A) and 1/F as a function of D/N (Figure S6B), unveiled the points of inflection at D/N = 2.0 and 1.0. When potassium ions are present the slope of N-2DEA fluorescence (F) as a function of wHTel-26 DNA concentration, [DNA], changed at [DNA] = 3.5, and 7.0 μM (Figure S5A), corresponding to D/N = 1.0, and 2.0, respectively. Inflection points were discovered

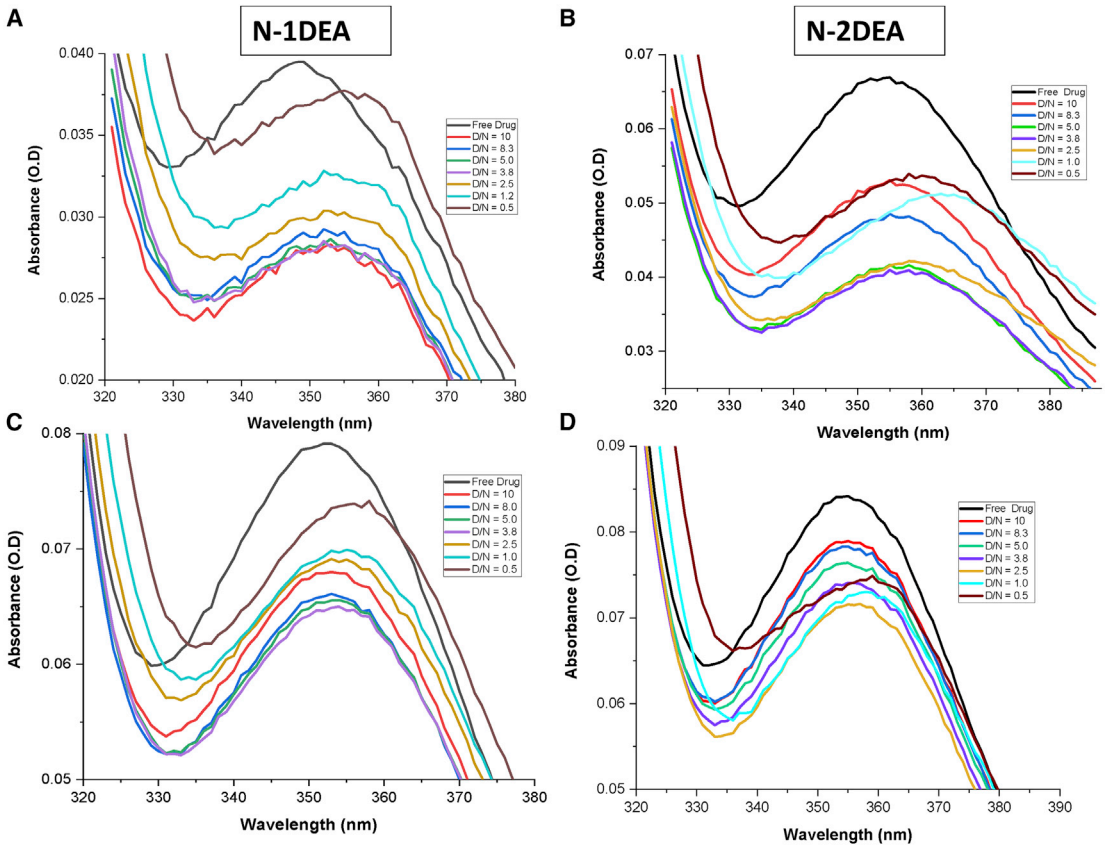

Figure 2. Absorbance spectra of 5 μM N-1DEA and N-2DEA

Absorbance spectra of 5 μM (A) N-1DEA and (B) N-2DEA with increasing concentration of wHTel-26 DNA from D/N = 0.5–10.0 in KBPES of 10 mM containing 100 mM KCl (C) N-1DEA and (D) N-2DEA with increasing concentration of HTel-22 DNA from D/N = 0.5–10.0 in NaBPES 10 mM containing 100 mM NaCl at 25°C, respectively.

at D/N = 1.0, and 2.0 as a function of D/N and reciprocal fluorescence, 1/F (Figure S5B), indicating stoichiometry is 1:1, 2:1. Using the Origin 2018 Pro software, we sought to fit the fluorescence data while function of DNA concentration into three alternative models: sequential and simultaneous binding at two different positions and a single binding site. Nonlinear curve fitting of both ligands in the presence of Na^+/K^+ to DNA complex revealed a satisfactory fit in two separate binding sites demonstrated a significant fit in two binding sites yielding two binding constants. The bimolecular quenching constant and stern-Volmer equation was also obtained from the Origin 2018 Pro software of both the ligands, and the values were given in (Figures S3–S6). By comparing the two molecules, we can conclude that human telomeric DNA has a different binding constant in the presence of K^+ rather than Na^+ ions. The fluorescence intensity of the N-2DEA DNA complex is quenched up to 91–95%, with a redshift $\Delta\lambda_{em}$ = 2–4 nm in both emission maxima indicating strong external binding interaction comparing N-1DEA ligand. The extremely efficient fluorescence quenching upon addition of DNA (Figure 3) suggests that small molecules are in close proximity to guanines with a favourable electron transport configuration, potentially as a result of partial chromophore insertion, resulting in partial stacking and a minor redshift around λ_{em} = 10 nm in case of N-2DEA titration with both the DNA.[36] Classical intercalation, on the other hand, would have efficiently screened the ligand molecule for quenching. End stacking/partial stacking of molecules may result via quenching of fluorescence strongly external binding, maybe followed by a minimal redshift in absorption and fluorescence. Because of the presence of many complexes, no isoemissive point was observed, as was the case with absorbance.

Stoichiometry estimation and fluorescence decay profile

We used an independent approach of continuous variation (Job plot) to achieve a direct estimation of stoichiometry because the fluorescence and absorbance data revealed the possibility of numerous stoichiometry complexes. In the presence of K^+ ions, variations in fluorescence intensity as a function of wHTel-26 DNA and N-1DEA mole fraction complex revealed inflection points at 0.5/0.8 (Figure S7A), resulting in 1:1/4:1 stoichiometry.[21,35,37] Inflection was also discovered in the N-1DEA HTel-22 sodium solution, demonstrating the possibility of 0.5:1 and 1:1 in the presence of sodium ions as inflection points shown at 0.32/0.5 (Figure S7C). The data

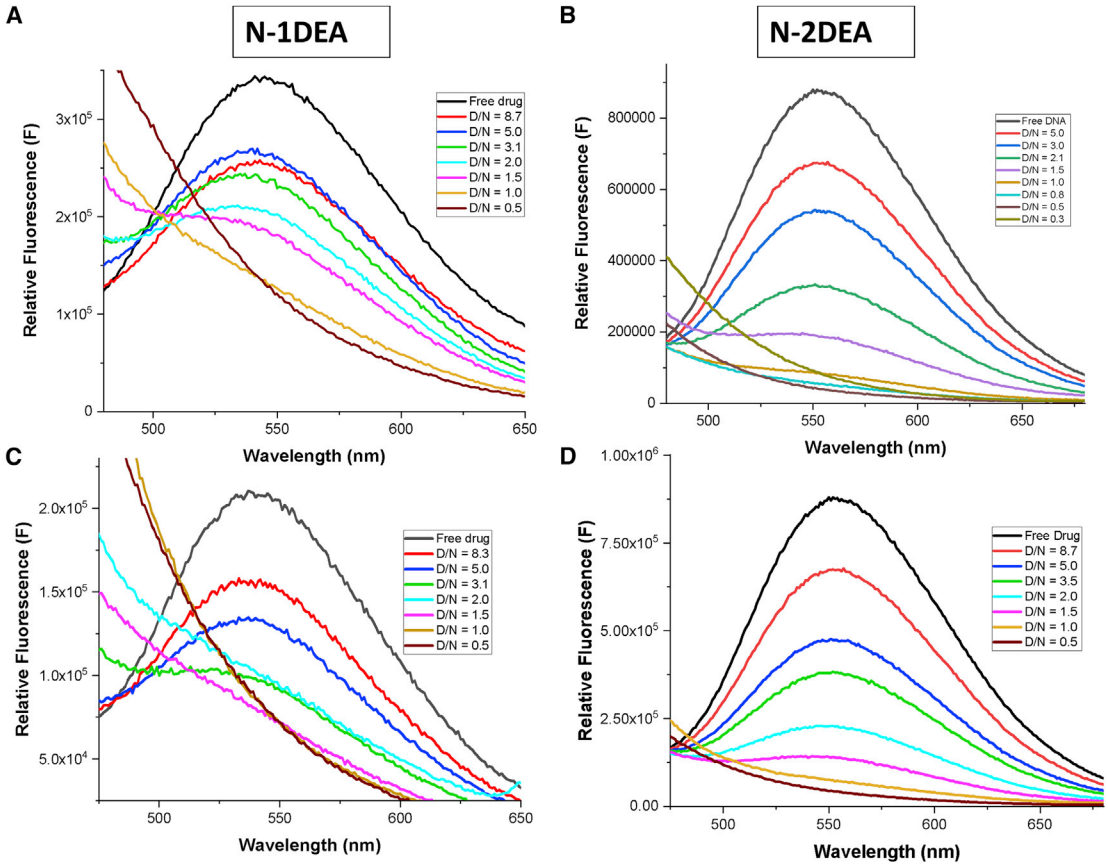

Figure 3. Fluorescence spectra at 5 μM N-1DEA and N-2DEA

Spectra of fluorescence of 5 μM (A) N-1DEA and (B) N-2DEA with increasing concentration of wHTel-26 DNA from D/N = 0.5–8.7 in KBPES (10 mM) containing 100 mM KCl with λ_{ex} = 352 nm and λ_{ex} = 354 nm; (C) N-1DEA and (D) N-2DEA with increasing concentration of HTel-22 DNA from D/N = 0.5–8.7 in NaBPES (10 mM) buffer containing 100 mM NaCl with λ_{ex} = 348 nm and λ_{ex} = 351 nm at 25°C, respectively.

of the N-2DEA complex shows inflection points in fluorescence intensity as a function of HTel-22 DNA, and the mole fraction of N-2DEA was found to be 0.5/0.66 (Figure S7D) in the presence of sodium ions, and 0.5/0.65 in the presence of potassium ions (Figures 4 and S7B), resulting in 1:1/2:1 stoichiometry. This stoichiometry is supported by similar trends in absorption and emission data.

Time-resolved fluorescence analysis emplyoing the fluorescence decay profile can show the binding process of the ligand-DNA complex. Fluorescence lifetimes of free and bound chromophores vary widely and can be determined experimentally. As demonstrated in Tables S4 and S5, the decay profiles are tri-exponentially fitted, providing two sets of average lifetime values at D/N = 1.0–4.0 (Figure S8), which can be attributed to the existence of three species.[38] This lifetime value is attributed to the complex being externally coupled with quadruplex and ruling out the intercalation hypothesis, which leads to a three-to four-fold increase in the ligand's lifespan compared with when it is free.[38] The decrease in fluorescence lifetime and photon release with increasing quencher concentration shows that the complex's excited state has been statically quenched by the drug and the K^+-rich solution. The assessed decay time constants of the complex show that K^+ and both ligands better stabilize the quadruplex.[39] The degradation profiles indicated the longevity in free and bound N-1DEA and N-2DEA complexes at D/N = 1.0–4.0 (Tables S4 and S5). The decay period of bound complexes in a K^+-rich solution is significantly smaller than that of unbound species, which could be attributed to the two types of binding nature seen in both complexes.[39]

Structural changes of G-quadruplex in the presence of Na^+/K^+ ions

To confirm the aforesaid interaction, we studied the structural changes caused by both ligands on wHTel-26 and HTel-22 DNA. Circular dichroism (CD) spectra discriminate G-quadruplex DNA with anti or syn-glycosidic bond angles. Parallel G-quadruplexes with anti-glycosidic bond shape yield positive guanine peaks at 264 and 240 nm.[40–43] Antiparallel G-quadruplex strands rich in guanines, with alternate syn- and anti-conformation in each DNA strand, have a significant positive peak at 245 and 292 nm and a trough peak at 265 nm, as seen in the 2+2 basket structure of the HTel-22 in Na^+-rich solution.[40–43] The wHTel-26 human telomeric sequence, flanked by TT and AA at the 3′ and 5′ ends

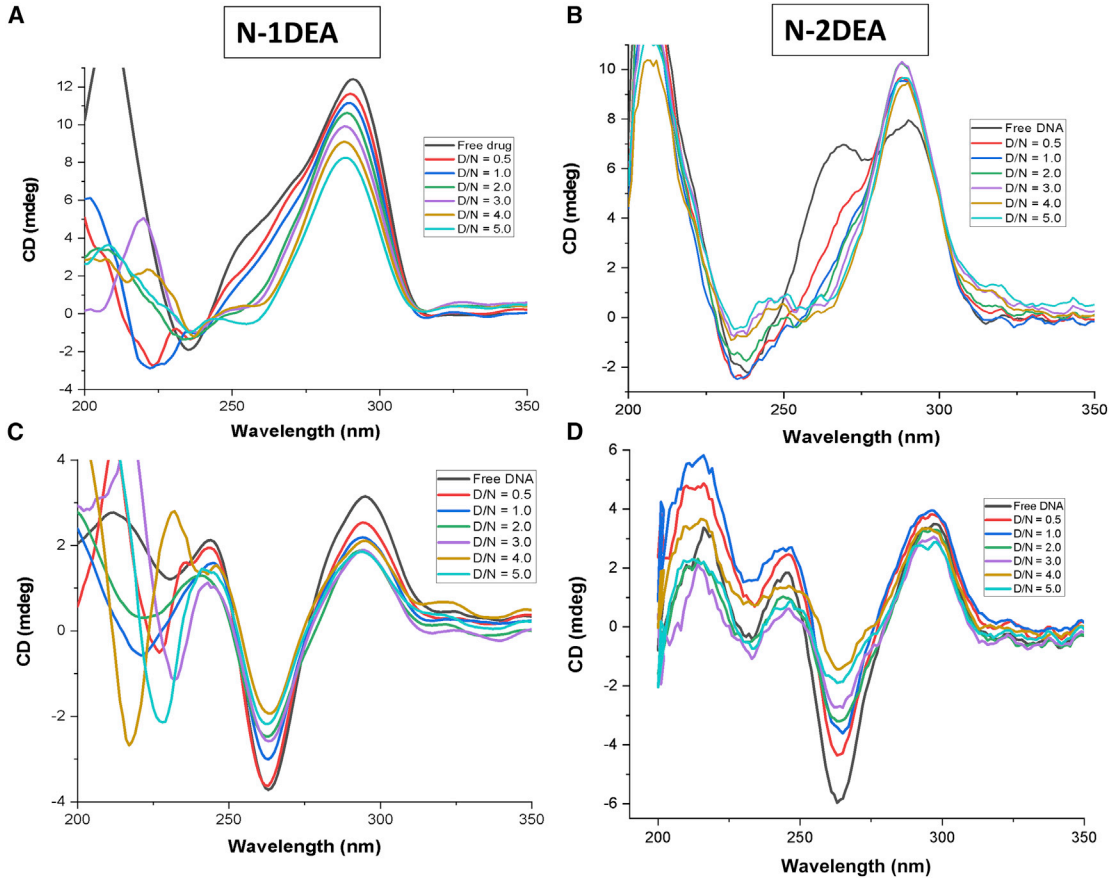

Figure 4. CD spectra of 20 μM free wHTel-26 in KBPES/NaBPES buffer have 100 mM KCl

Titrations of 20 μM wHTel-26 on progressive addition of (A) N-1DEA and (B) N-2DEA at D/N ratio = 0.5–5.0 in KBPES buffer with wHTel-26 titrations of 20 μM HTel-22 on successive addition of (C) N-1DEA and (D) N-2DEA at D/N ratio = 0.5–5.0 in NaBPES containing 100 mM NaCl buffer with fixed HTel-22 (20 μM) DNA.

of the 22-mer sequence, has a well-defined stable 3+1 hybrid structure in K^+-rich solutions that differ in loop creation with double chain reversal. This precise conformation is known as form 1 and forms 2, and it is formed by the first and third linkers, respectively.[44] Because of the change in syn- and anti-glycosidic conformation between the middle and top G-tetrads, the wHTel-26-mer sequence flanked by TT bases creates a strong positive CD band at 290 nm, called a hybrid form 2 structures in potassium-rich solution. It features a positive shoulder around 264 nm and a tiny negative band around 240 nm, typical of anti-glycosidic bond rotation between bottom and middle G-tetrads.[6,40–43]

The significance of the CD band at 264 and 292 nm decreased considerably after adding N-1DEA to wHTel-26 DNA fix at 20 μM wHTel-26 containing 100 mM K^+ (Figures 4A and 4B) because of relative changes in the conformation of two G-quadruplex forms. The ellipticity shift is minor, and the overall shape of the CD band remains unchanged. This characteristics exclude typical intercalating as a binding technique and suggests that both ligands bind to DNA externally.[21,27] The ellipticity of wHTel-26 DNA reduced dramatically after adding N-1DEA at the 264 and 292 nm peaks; however, after adding N-2DEA, the 264 nm peaks progressively declined, while the 292 nm peaks gradually grew and stabilized at D/N = 0.5–5.0. The progressive addition of both ligands to 20 μM wHTel-26 reduces the intensity of the positive bands at 264 nm by 33% and 80%, respectively (Figures 4A and 4B), with a maximum redshift of 3 nm in both CD bands at D/N = 5.0. This demonstrates a significant external contact between the ligand and the DNA molecules.

We evaluated the impact of sodium ions on the folding of the HTel-22 sequence, which folds an intramolecular G-quadruplex 2+2 basket-type structure along with one diagonal loop and two sides with anti-parallel guanine-molecule arrangements.[45] In addition to the ligands at 20 μM HTel-22, the significance of CD bands at 292 and 264 nm for both molecules rapidly diminished (Figures 4C and 4D). In the presence of Na^+/K^+ ions, nonlinear fitting of the wHTel-26 and HTel-22 ligands revealed a consistent affinity at different wavelengths (Figure S9). As a result, in the presence of K^+ ions, the binding affinities of N-1DEA are one order higher than those of N-2DEA (Figure S9). The absence of an induced CD band in each case could be attributed to the presence of several complexes. As a

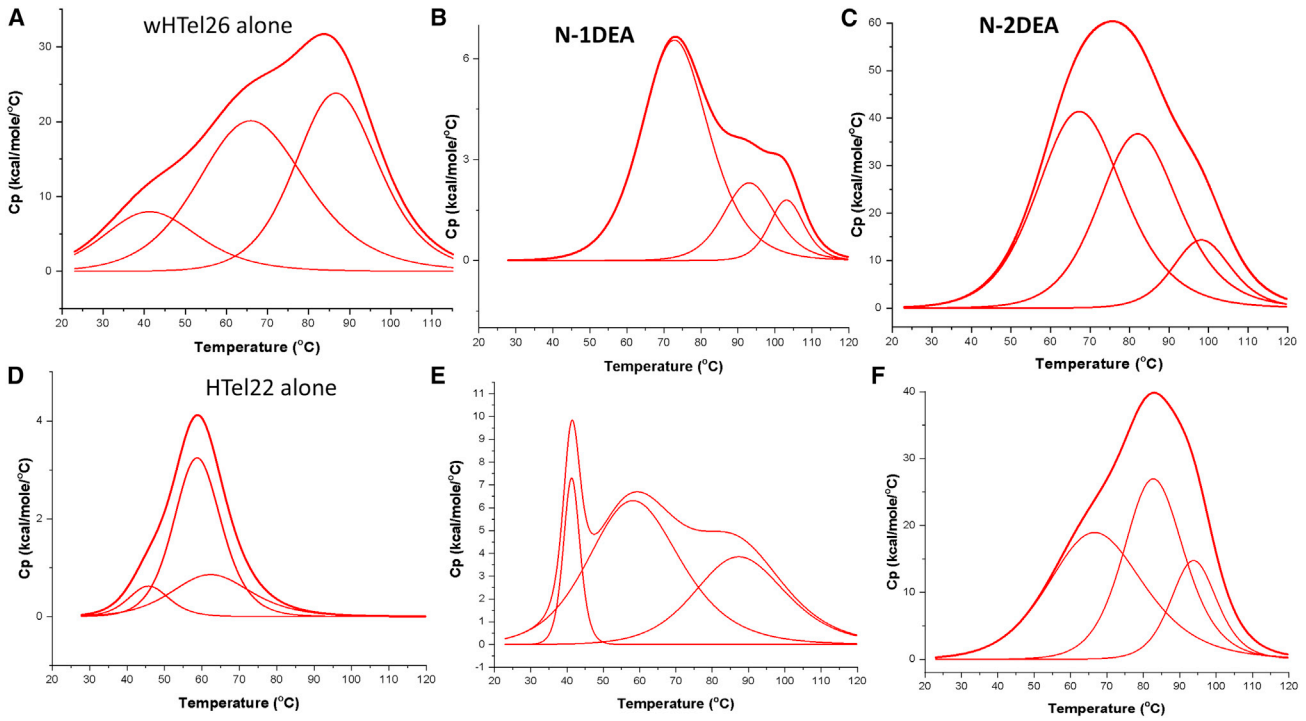

Figure 5. Thermal melting profiles showing excess heat capacity as a function of temperature

For (A) 100 μM free d[TT(AGGGTT)$_4$]; (B) its complex with N-1DEA; (C) N-2DEA at D/N ratio = 5.0, in presence of 100 mM KCL; (D) 100 μM free [d-AGGG(TTAGGG)$_3$] (E) its complex with N-1DEA; (F) N-2DEA at D/N ratio = 5.0, in the presence of 100 mM NaCl. The observed raw data (thick black lines) in each figure has been deconvoluted into three "two-state" processes (thin gray lines) using Origin 7.0.

result, end stacking as well as groove binding may be responsible for ligand extrinsic DNA binding in the present work.[30,35]

Thermodynamic stabilization of both the G-quadruplex DNA in the presence of anthraquinone derivatives

The change from G-quadruplex to disordered DNA contains various intermediates along the journey that relate to partially folded and partially unfolded states.[46] The temperature at which DNA is unwound from its folding state is referred as the hypothetical melting temperature (T_m). A differential calorimetric scanning method was used in measuring the melting profile (T_m) of quadruplex structure at D/N = 0 and 5.0 separately. These data are fitted in the 3-state wHTel-26 free 80 μM DNA melting curve. Figure 5A shows that the melting temperatures of free wHTel-26 DNA with T_{m1}, T_{m2}, and T_{m3} centers are 42.0°C, 66.8°C, and 87.2°C, respectively, implying the presence of three melting species. Similarly, three transitions of T_{m1}, T_{m2}, and T_{m3} at 45.9°C, 59.0°C, and 62.9°C (Figure 5D), respectively, give rise to HTel-22 at 50 μM concentration. The transition of thermal profile (ΔT_m) indicates a $\Delta T_m \sim$ 1.7°C, 7.1°C from the N-1DEA complex (Figure 5B), and 1.2°C, 11.2°C, and 15.8°C from the N-2DEA complex with wHTel-26 (Figure 5C) being observed after binding at D/N = 5.0. Conversely, an N-1DEA complex shows $\Delta T_m \sim$ 25.2°C (Figure 5E) and 8.6°C, 20.1°C, and 31.1°C stabilization with N-2DEA and HTel-22 DNA complex at D/N = 5.0, as seen by the difference in melting profiles (Figure 5F). Furthermore, the thermograms could not be fitted in two "two-state" models using Origin software. We chose "three-state" models since they yielded a lower value of χ^2 on thermogram fitting, yielding three melting transitions (Table 1). Different fitted graphs depict different bound complex conformations with lower relative concentrations than the principal conformer. Thermal stability is raised by 20°C by a known RHPS4-binding G-quadruplex intercalator. Other groove binding units, such as analog peiminine and quinine,[47] furan derivatives,[48] raise the T_m of human telomeric DNA by 13°C–14°C. Groove-binding ligands increase the stability of quadruplex DNA. Because of structural differences, both ligands may bind to DNA and stabilize HTel-22 more than wHTel-26 in the presence of sodium ions in our investigation.

CD analysis determined the structure-related melting temperature at 290 of both peaks, with folded to unfolded N-1DEA and N-2DEA to both the wHTel-26 and HTel-22 G-quadruplex DNA native to the complex states of D/N = 0 and 5.0. The DSC thermogram and CD experiment differ in that we received three thermograms in DSC, and the CD trials were performed at 2°C interval. Structure changes in melting tests have been noticed differently in the CD peak at 290 nm. The CD of free HTel-22 and wHTel-26 in the presence of Na^+ and K^+ measured at 291 nm concerning temperature (Figure S10) revealed a major peak at 61°C, which increased to 73°C and 76°C–90°C (±2°C) with the addition of N-1DEA with wHTel-26 at D/N = 5.0, as shown in the plot of CD derivative concerning temperature (Figure S10A). When D/N = 5.0, a positive hump was also

Table 1. Melting temperature T_m (°C) of d[TT(AGGGTT)$_4$] in free and bound with N-1DEA + wHTel-26 and N-2DEA + wHTel-26, respectively

No	D/N	T_m1	ΔT_m1	T_m2	ΔT_m2	T_m3	ΔT_m3	T_m4	ΔT_m4	Chi square/DOF
A	0	42.0 ± 1.3	–	66.8 ± 0.7		66.8 ± 0.7	–	87.2 ± 0.3	–	6.6×10^5
B	5	–	–	68.5 ± 1.1	1.7	73.9 ± 0.5	7.1	79.4 ± 1.6	–	3.5×10^4
C	5		–	68 ± 0.5	1.2	82.6 ± 0.3	15.8	98.4 ± 0.4	11.2	6.5×10^5
D	0	45.9 ± 0.5	–	58.9 ± 0.1	–	62.9 ± 3.6	–	62.9 ± 3.6	–	6.6×10^5
E	5	41.3 ± 0.0	–	59.0 ± 0.3	1	–	–	88.1 ± 0.3	25.2	1.2×10^5
F	5	–	–	67.5 ± 1.0	8.6	83.1 ± 0.6	20.1	94.0 ± 0.5	31.1	5.4×10^5

Melting temperature T_m (°C) of (A) d[TT(AGGGTT)$_4$] in free and bound (B) N-1DEA + wHTel-26; (C) N-2DEA + wHTel-26, in presence of K^+ at D/N = 5.0 (D) [d-AGGG(T-TAGGG)$_3$] G4 DNA in free form, and complex with (E) N-1DEA + HTel-22, (F) N-2DEA + HTel-22, in presence of Na^+ by fitting data into three "two-state" transition model using differential scanning calorimetry (DSC) data.
Changes in melting temperature, ΔT_m (°C), and χ^2 for the goodness of fit are also shown.

observed at 73°C. The results for the N-2DEA and wHTel-26 complex were comparable (Figure S10B), indicating thermal stability at T_m 10°C–13°C (±2°C). Thermal stability was demonstrated in the presence of 100 mM NaCl when N-1DEA (Figure S10C) and N-2DEA (Figure S10D) were bound at a molar ratio of 5.0. The CD melting profile (Tables S6 and S7), like the DSC thermogram, revealed that sodium ions give more stability to the G-quadruplex complex than K^+ ions.

We next used calorimetric titration to study the heat exchange profiles of both ligands for the G4 synthesis of wHTel-26 oligos. The results showed that the enthalpy changes (ΔH) in potassium ions caused by the combination of wHTel-26 DNA were significantly negative and exhibited an energy advantageous for N-1DEA and N-2DEA binding (Figure S11). Using ITC 200 Origin software, all data were fitted in sequential binding sites. Both ligands have an exothermic interaction with wHTel-26 DNA in the presence of potassium ions, but N-2DEA has an exothermic followed by an endothermic reaction. These isotherms demonstrated that the interaction of N-1DEA and N-2DEA with G-quadruplex DNA with micromolar affinity is thermodynamically stable and specific. Calculating the enthalpy (ΔH), entropy (ΔS) and binding affinity (K_b) in the situation of two small molecules interacting with the wHTel-26 sequence (Tables S8 and S9) leads to the conclusion that the reaction is favorable and strong with no non-specific binding. The coupling of favorable/unfavorable enthalpy and entropic variables indicates multiple ligands binding to quadruplex structures, supporting the above spectroscopic data.

Cell-based assay

Cell viability

At 24 h test on the MCF-7 (breast cancer cell), cancer cell lines in identical conditions were determined for short-term cell viability assay. In MCF-7 cells with half maximal inhibitory concentration (IC_{50}) values of 3.4 and 1.3 μM, for N-1DEA and N-2DEA (Figure S14), the cytological compound behavior was observed at low micromolar concentrations.

Cell morphology visualization

We assessed changes in cellular morphology to see how the drug affected them. When ligands (N-1DEA and N-2DEA) were incubated in cells at the IC_{50} dose, MCF-7 cells displayed normal chromatin condensation as the nuclei shrank in size compared with healthy control cells (Figure 6A) at 12, 24, and 48 h. This result showed that the chemicals caused nuclear morphological alterations (arrow line) during apoptotic cell death. Condensation, nucleus fragmentation, and cytoskeleton disturbances were observed in MCF-7 cells treated with the chemical, indicating apoptosis (Figure S12). Both Figures 6A and S12 are the same. Morphological changes suggested that the cell was undergoing apoptosis. Fluorescence microscopy studies of their cellular mobility could give new information on the mechanism of action of these anti-cancer therapies in the future. Because of the morphological changes and cell death during treatment, we hypothesized that this might be due to the apoptosis that is induced by the drug treatment. To assess the apoptosis, we checked the expression level of caspase-3 by western blot. The expression of caspase-3 was highly induced in the drug-treated samples, whereas no caspase-3 expression was observed in the untreated samples at the indicated time points (Figure S13). This suggests that the morphological change is due to apoptosis.

According to our findings, ROS induction is highly significant after treatment with both drugs (Figures 6C and 6D). Nonetheless, effective/specific drug binding causes oxidative stress in cancer cells, which leads to cell death or apoptosis/necrosis. Our findings strongly decipher that after 24 h of treatment, these drugs generate considerably more ROS in cancer cells than untreated cells, leading to cell apoptosis.

Furthermore, the living dead (Annexin V-FITC/PI) dual-labeling experiment was used to evaluate the cell death process. We can use this assay to determine the percentage of living, apoptotic, and necrotic cells. Flow cytometry analysis reveals a large number of apoptotic cells after 12, 24, and 48 h of incubation with the chemicals. The fluorescence-activated cell sorting (FACS) pictures divide the cell population into four quadrants, with live cells in the lower left (LL) indicating the presence of live cells and dead cells in the upper left (UL) indicating the presence of dead cells. Instead, the upper right (UR) and lower right (LR) quadrants distinguish between cells in early and late apoptosis. As evidenced by the distribution of cells in the LR and UR quadrants, apoptosis was detected in MCF-7 cells after 12, 24, and 48 h of treatment with IC_{50} similar doses of N-1DEA and N-2DEA (Figure 7). The

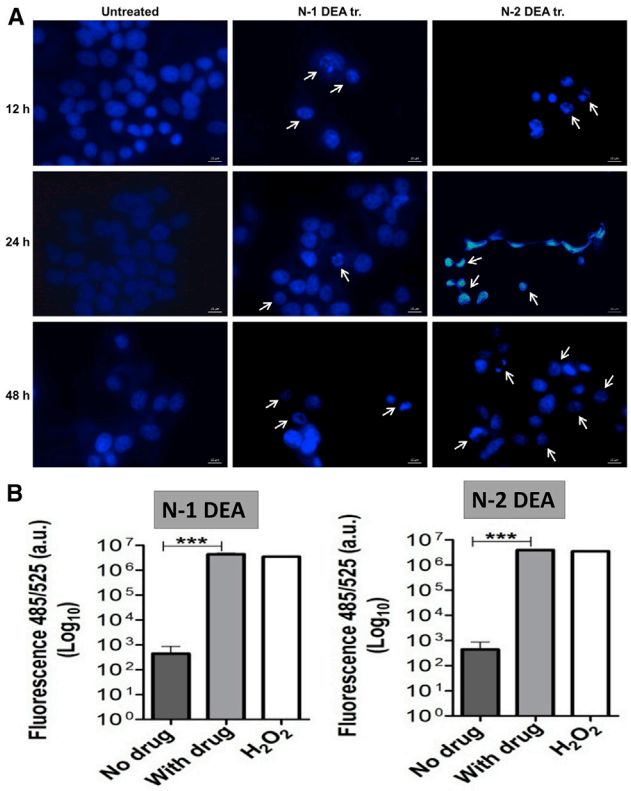

Figure 6. Fluorescence microscopy images of the condensed nucleus and Log plot of ROS estimation after treatment of N-1DEA and N-2DEA, respectively

Fluorescence microscopy images of the condensed nucleus after treatment of (A) N-1DEA and N-2DEA compound (scale bar, 10 μm) after treatment with N-1DEA and N-2DEA at 12, 24, and 48 h (scale bar, 10 μm) which stained with Hoeschst 33342 (blue color). Control cells represent untreated cells. (B) Log plot of ROS estimation after treatment of N-1DEA and N-2DEA, respectively. H_2O_2 is taken as a positive control.

percentage of total late apoptotic cells for individual treated cells for 12 h at IC_{50} similar doses was determined to be 19.94% (for N-1DEA) and 12.01% (for N-2DEA) compared with untreated cells, as shown in the following diagram. But for 24 h at IC_{50} similar doses late apoptotic cells increased up to 23.33% (for N-1DEA) and 59.16% (for N-2DEA) compared with untreated cells.But at 48 h treatment of ligands N-2DEA had a substantially larger percentage of necrotic cells (75.58%) than N-1DEA (29.12%). In this time point N-1DEA treated cells undergoes in early apoptotic stage about 35.37%.

Transcriptional regulation study

Additionally, we explore the influence of N-1DEA and N-2DEA on the qRT-PCR transcript of G4 motif-containing oncogenes (*c-MYC* and *BCL-2*). GAPDH (housekeeping gene) transcript gene transcripts were quantified, and the non-template control quantification cycle (CT) was 40 cycles (by default). Time-dependent treatment (12, 24, and 48 h) of MCF-7 cells with the IC_{50} value of both ligands down-regulating the oncogene transcript (inhibit promoter of *c-MYC* and *BCL-2*) (Figure S13). These findings suggest that a G4-mediated mechanism is involved in the transcription of G4-containing genes, opening up a novel therapeutic target for an oncogene.

Molecular interactions between N-1DEA/N-2DEA and DNA by docking

The molecular docking of N-1DEA and N-2DEA with different human telomeric DNA structures in the literature was performed to provide an insight into the binding mode, showing schemes and G-quartet residues in Figure S15.

In the presence of potassium and sodium ions, the human telomere sequence adopts various structural conformations. Form 1 consists of two lateral loops, and the first linker is a double chain reverser (PDB: 2HY9) however, form 2 differs from form 1 by incorporating a reversing double chain loop made up of the third linker (PDB: 2JPZ).[44,49] Sodium-ion solutions are provided in the form of a 2+2 parallel basket structure (PDB: 143D).[45]

The complex formation in form 1 of a 3+1 hybrid 2HY9 structure was supported, yielding the lowest N-1DEA energy binding energy of −9.92 kcal/mol (Figure 9A). Table S10 provides information on all polar contacts and residues implicated in hydrogen bonding. Alternatively, the binding to the 3+1 hybrid (form 2) 2JPZ structure was less energetically promising, with a binding energy of −8.16 kcal/mol (Figure S15). Although G-quadruplex in 2HY9 and 2JPZ hybrid structures is more readily available for end stacking, stacking interactions with any of them were not included in the binding. Interactions with any G-quartet were not necessary for the stacking processes of 2HY9 or 2JPZ, despite the fact that the final stacking structures were simpler. The 2JPZ binding processes are more efficient than the 2HY9 binding processes. G4 DNA of 143D anti-parallel 2+2 two ligands has a distinct structure and is more common in Na^+-rich conditions. When paired with 2+2 parallel structures and 4 polar contacts of quadruplex DNA's G14 and A13 are linked to N-1DEA atoms, 143D had a binding energy of −8.53 kcal/mol (Figure S15). N-2DEA binding energy appears to be increasing in the order 143D < 2JPZ < 2HY9 (Figure S15D–S15F). This is supported by observations that N-2DEA promotes anti-parallel structure more than N-1DEA. The outer G-tetrads are largely buried in this structure compared with 3+1 hybrid structures that suit the hose type; ligands and stacked structures are not likely to interact. Despite G-quadruplex are more readily available for end stacking in 2HY9 and 2JPZ hybrid structures, stacking interactions with any of them were not included in the binding. Interactions were not required for the stacking processes of 2HY9 or 2JPZ with any G-quartet, despite the fact that the end stacking structures were more accessible. The first and second lateral loops were joined, and N-2DEA was connected to the third strand.[42,50]

DISCUSSION

It is notable that data reinforce the SPR binding data, implying that the greater binding affinity is due to both compounds' additional interaction with the quadruplexes. The findings show that the quadruplex could augment ligand binding affinity by leveraging additional

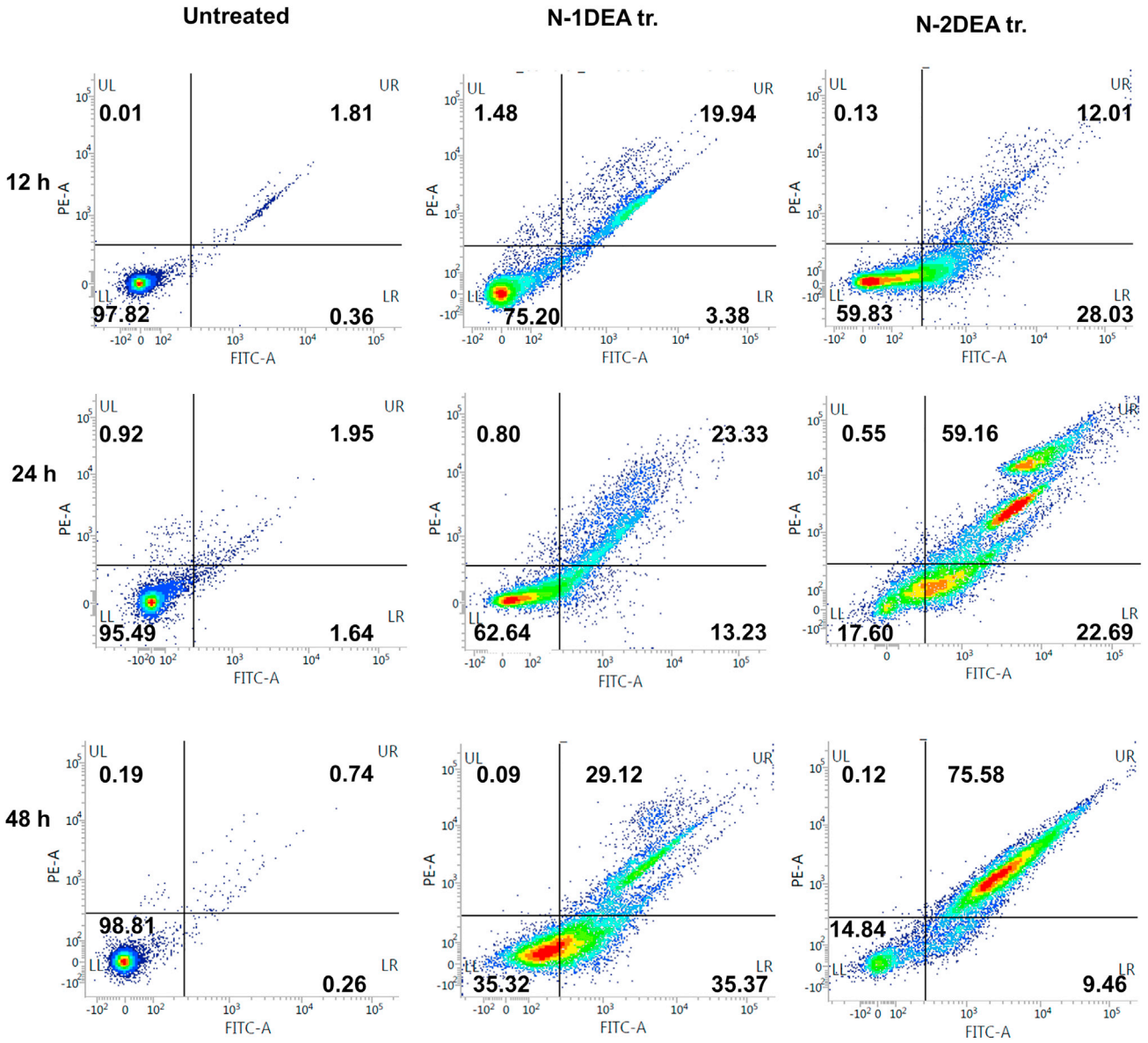

Figure 7. Bar graph of FACS analysis using annexin V and PI staining of control (untreated) cells N-1DEA treated and N-2DEA, respectively

contact with the groove. Second, the interaction rule out the feature of end stacking binding through any base quartet, that is consistent with small redshift in excitation and emission maxima that have been observed previously.[51] Electrostatic coupling, on the other hand, is shown by low or no changes in fluorescence and CD spectra. Fluorescence measurements intensity show strong quenching and a minor redshift, indicating stacking at the top or bottom of the tetrad or near G-tetrads along the DNA backbone.[52] As a result, in the present study, both end stacking and groove binding may be responsible for drug to external DNA binding. The circular dichroism spectra show that the overall DNA shape remains unchanged, with parallel/anti-parallel stranded strands stacking base quartets in the same way that free DNA quadruplex and right handed helix geometries do. Meanwhile, the present findings show that N-2DEA binding to G-quadruplex grooves increases thermal stability by around more than 25°C that may inhibit telomerase, indicating that this is a promising strategy for generating highly selective G-quadruplex targeting therapies.[53] Docking-based studies concentrate on specific chemical entities of ligands involved in interactions that are regulated by both the type of ligand and the complexity of the G4 structures. The side chains of ligands dictate their binding properties, which can hang in grooves or adhere to the DNA backbone by hydrogen bonding, van der Waal or hydrophobic interactions. As any aromatic chromophore can stack with G-quartet because stacking interactions

are non-specific. The observed thermal stabilization could be the result of ligand-specific binding, which caused conformational changes or a substantial prevalence of parallel/anti-parallel/hybrid structures in CD spectra. Because of conformational differences, binding with pure anti-parallel structure in Na^+-rich solution stabilizes more than K^+. Although G4 DNA grooves are different from duplex DNA grooves and adopt variable conformations depending on cation type (K^+/Na^+) and concentration in physiological state this property can be used for structure-based drug design.[54] Both the ligands could be part of a signaling process that uses ROS as secondary messengers to control transcription by turning on DNA repair processes, especially base excision repair, has been previously reported. Nuclear condensation mimics the effects of oxidative stress as a possible reciprocal mechanism for DNA damage repair and triggering cell senescence induced by both small molecules.[55] The new study further demonstrates that direct drug-DNA binding promotes thermal stabilization, which may lead to inhibition of interaction of telomeric DNA with telomerase and therefore, reduced functionality of telomere. Following strong binding of both ligands, cellular assays demonstrated growth inhibition, cellular shape perturbation, and nuclear condensation in cancer cells.

Conclusions

We demonstrated extensive interactions with multiple G4 DNAs with synthesized substituted anthraquinone derivatives tagged with a diethyl group. According to a real-time binding and steady-state kinetics study, the N-2DEA molecule binds more specifically than N-1DEA. SPR verifies the presence of d-[AGGG(TTAGGG)$_3$] with N-1DEA and N-2DEA, with K_b values of 5.4×10^5 M^{-1} and 1.6×10^6 M^{-1}, respectively. Relevant binding affinities, changes in ellipticity, the hypochromic shift of absorption spectra, and quenching in steady-state fluorescence studies all contribute to the stacking or groove binding mode. Thermal profiling suggests that sodium ions contribute high stability to G4 and N-2DEA complexes compared with G4 and N-1DEA complexes. External binding in G4 DNA grooves and loops was established by molecular docking without direct interaction with DNA bases. According to the results of cumulative biophysical investigations, substantial binding of the G-quadruplex with both molecules resulted in efficient thermodynamic stability and energetically favourable.

Furthermore, nuclear condensation reveals cellular morphology changes after treatment with both the ligand. High ROS levels reflect cell senescence which is linked to telomere attrition. On the basis of their inhibitory concentrations, both compounds with diethyl analogs may be more promising than the mother molecule in the future for targeting and stabilizing G4 DNA for anti-cancer therapy.

MATERIALS AND METHODS

Synthesis

General procedure for synthesis of 2, 6-bis[3-(diethylamino) acetamido]anthracene-9,10-dione

A suspension of 2, 6-diaminoanthraquinone in freshly distilled chloroacetyl chloride (N = 1) was refluxed for 5 h until TLC indicated completion of the reaction. After cooling to 0°C–5°C, the mixture was filtered and the solids were washed with ether and 1,4-dioxane. Recrystallization from EtOH afforded 2, 6-bis(chloroacetamido)anthracene-9,10-dione (I1) as yellow prisms. Chloroacetamide (I1) above prepared was then treated with excess diethylamine in EtOH. After 5 h of reflux, at which time the reaction was judged (TLC) to have reached completion, the solution was chilled to 0°C–5°C. The solid that separated was removed by filtration washed thoroughly with ether, digested in $CHCl_3$, and treated with decolorizing charcoal. Recrystallization from EtOH gave us 2, 6-bis[3-(diethylamino)acetamido]anthracene-9,10-dione(N-1DEA) as crystals (Figure S16). Nuclear magnetic resonance (NMR): δ(DMSO): 1.03 (t, 12H, NCH_2CH_3), 2.63 (q, 8H, NCH_2CH_3), 3.26 (s, 4H, $COCH_2$), 8.16 (d, 2H, H-3,7), 8.16 (d, 4H, H-4,8), 8.56 (s, 2H, H-1,5), and 10.31 (s, 2H, NH).[56]

General procedure for synthesis of 2, 6-bis[3-(diethylamino) propionamido] anthracene-9,10-dione:

A suspension of 2, 6-diaminoanthraquinone in freshly distilled 3-chloropropanoyl chloride (N = 2) was refluxed for 5 h until TLC indicated completion of the reaction. After cooling to 0°C–5°C, the mixture was filtered and the solids were washed with ether and 1, 4-dioxane. Recrystallization from DMF-EtOH (4:1) afforded 2, 6-bis(3-chloropropionamido)anthracene-9,10-dione (I2) as orange crystals. Diethylamine was added to a refluxing suspension of propionamide (I2) in EtOH and the reaction mixture was refluxed for 5 h. After the completion of the reaction, the reaction mixture was chilled to 0°C–5°C, and the solid compound was separated, washed with ether, digested with $CHCl_3$, treated with decolorizing charcoal, and filtered. Recrystallization with DMF-EtOH afforded 2, 6-bis[3-(diethylamino)propionamido] anthracene-9,10-dione(N-2DEA) as yellow-brown crystals (Figure S16). NMR: δ(DMSO): 1.30–1.42 (m, 4H, $N[CH_2]_2CH_2$), 1.55–1.58 (m, 8H, NCH_2CH_2), 2.46–2.50 (m, 8H, NCH_2CH_2), 3.16 (s, 4H, $COCH_2$), 8.14 (dd, J = 8.0 Hz, J = 2.1 Hz, 2H, H-3,7),8.17 (d, J = 8.0 Hz, 2H, H-4,8), 8.54 (d, J = 2.1 Hz, 2H, H-1,5), and 10.39 (s, 2H, NH). Both derivative NMR peaks show a strong resemblance to prior literature, implying that the purity level is high.[56]

Oligonucleotides sequences

All desalted oligonucleotides sequences, primers as well as the 5′ biotin-labeled, desalted nucleotide sequenced-[AGGG(TTAGGG)$_3$] were purchased from Sigma-Aldrich (Table S1). All oligonucleotide stock solutions were prepared using molar extension coefficient at absorption spectra in 260 nm.

Spectroscopic analysis

In absorption, CD and fluorescence spectroscopy experiments, while stock solutions were prepared in newly prepared 10 mM phosphate (KBEPS = 10 mM K_2HPO_4, 100 mM KCl and 1 mM EDTA) and NaBPES = 100 mM NaCl, Na_2HPO_4 10 mM, 1 mM EDTA) buffer in the set of experiments (pH 7.0). Testing of SPR was carried out using the Biacore T200 instrument (optical biosensor system made by GE Healthcare, Chicago, IL) according to conventional protocols.[28–30] 10 nM 5′ biotin-labeled d-[AGGG(TTAGGG)$_3$] was diluted

in HEPES buffer (100 mM KCl, 0.01 mM HEPES, 3 mM EDTA and 0.05% (v/v) surfactant P20), then immobilization process was done on a derivatized streptavidin sensor chip purchased from BIACORE SA, make GE Healthcare Life Sciences, UK). Using Biacore T200 assessment software, data were fitted and analyzed to determine the affinity constant (K_b).

The absorbance measurements were made with a CARY-100 Bio UV–visible spectrophotometer fitted with a thermostatic cell holder (Varian), and the binding constant (K_b) was determined using established equations.[21] Fluorescence studies were performed at 25°C in the emission range λ_{em} = 500–680 nm using an excitation wavelength of 355 nm on a Fluorolog-3 Spectrofluorimeter LS55 (make Horiba Jobin Yvon Spex). The binding constant was estimated using a user-defined equation created in Origin 2018 Pro to fit the data into a nonlinear curve fitting regression analysis. Using an approach reported earlier the Stern-Volmer quenching constant (K_{SV}), binding constant (K_b), and complex stoichiometry (n) were also estimated.[30] Fluorescence at 25°C, using a 1 cm quartz cuvette, lifetime measurements were performed for 5 μM free N-1DEA/N-2DEA and their complexes at different drug/nucleic acid (D/N) ratios (making by Horiba Jobin Yvon Spex Fluoro-Cube fluorescence lifetime system) in time-correlated single-photon counting (TCSPC) mode and equipped with nanosecond time domain. The data were fitted using the DAS 6.3 software's re-convolution method, which produces the finest fit chi-square values. Continuous variation job plots were used to assess complex stoichiometry by monitoring the fluorescence of samples with total DNA and ligand concentrations fixed at 5 μM and relative molar fractions varied at 0.05 intervals.[28–30] CD studies were carried out on a Jasco J-1500 CD spectrometer equipped with a Mini circulation MCB-100 using standard parameters and the affinity constant was calculated using nonlinear data fitting.[28–30] Melting profiles of 20 μM free DNA and melting transition of complexes were acquired by recording the CD spectrum as a function of temperature. To explore the thermal transition from bound quadruplex helix state to unbound state for 100 μM wHTel-26/HTel-22 and its complexes, a VP-DSC micro-calorimeter (Microcal Inc., Northampton, MA) were used to estimate the excess heat capacity as a function of temperature.[28–30] The thermograms were analyzed using Origin software integrated VP Viewer software. Autodock 4.2 was used for molecular docking ligands to G4 DNA, and Autodock Tools 1.5.6 was used to create multiple files using PDB IDs 2HY9, 2JPZ, and[44,49] 143D.[45]

Cell viability and cell-cycle arrest

MCF-7 cells (Mycoplasma free) purchased from NCBS (India) were seeded in a 96-well plate at a density of 1×10^3 cells per well. After 24 h of adhesion at 37°C and 5% CO_2, the cells were treated with various chemical solutions. After the incubation period, 20 mL of 5 mg/mL 3-(4,5-dimethylthiazol-2-yl)-2,5-diphenyltetrazolium bromide (MTT) solution was carefully added to each well and stored at 37°C for 4 h. After draining the supernatant, the formazan crystals generated at the bottom of the well were dissolved in DMSO (200 μL), and the absorbance was measured at 570 nm. The percentage of cell viability obtained by the following formula given below cell viability (%) = {[absorbance (570) of treated cells − absorbance (570) of plain DMSO]/[absorbance (570) of untreated cells − absorbance (570) of plain DMSO]} × 100.

ROS assay

Cells were plated at 2.5 × 104 per well in a 96-well plate. N-1DEA and N-2DEAwere treated with their IC_{50} concentration after 24 h of incubation. A 10 mM stock solution of DCFDA (Sigma) was produced in DMSO and diluted in RPMI (without FBS) to yield a working solution of 100 μM, with hydrogen peroxide (0.1 mM) used as a positive control cell. After exposing the cells to the drug for 24 h, the supernatant was discarded and the cells were rinsed in 1× PBS. The cells were then treated in the dark for 30 min with 1 mL of DCFDA working solution at 30°C. The identical condition was applied to control cells. The cells were then lysed with a trypsin-EDTA solution and centrifuged for 10 min at 2,000 rpm; 1 mL supernatant was ready for fluorescence emission measurement at 535 nm.

Fluorescence microscopy assay

First, seed cells at a density of 0.6×10^6 cells per plate on a coverslip in a 60 mm dish, and the drug were treated at the IC_{50} concentration. All slides cleaned twice with 1× PBS after 24 h. The cells were then fixed for 20 min at room temperature in cold paraformaldehyde (3.2%). Permiablized cells were then lysed for 5 min with 0.1% Triton X-100. After washing, cells were treated with Auto 488 phalloidin for 60 min, followed by 30 min of Hoeschst 33342 dye. Coverslip is ready for microscopy (Zeiss AXIO Scope A1) visualization.

Gene regulation assay

Cells were seeded in 24-well plates at a concentration of 2×10^4 cells and incubated at 37°C and 5% CO_2 for 24 h. Cells treated after 24 h of IC_{50} concentration and without treatment cells were taken as a control. All samples are prepared by the manufacture protocol of Takara. All RNA samples quantification was done using nanodrop (yield at A280/260). A 20 μ l reaction, reverse transcription was performed using the high capacity cDNA reverse transcription kit (Takara). qRT-PCR was then performed in a Quant studio Thermal Cycler using a PCR master reaction mix containing 1× iQ SYBR Green Master Mix (Applied Biosystems), 0.5 μM of each primer, and 1 μL of cDNA sample in a final reaction volume of 10 μL in a 96-well PCR plate. The CT values of GAPDH were used as a normalizing reference and as a measure of RNA integrity. Quant studio 5 software was used for analysis.

Isothermal titration calorimetry

Thermogram readings were taken from ITC 200 titration calorimeter (MicroCal). The solutions were degassed carefully before loading. The degassed buffer was poured into the reference cell. The quadruplex (40 μM) was retained in the sample cell, and the drug (1,000 μM) in KBEPS buffer was added in 1 μL aliquots at 120 s intervals at 25°C (for a total of 39 injections, each lasting 2 s). The temperatures of dilution were obtained in parallel studies in control experiments by injecting a 1 μL solution of the same concentration in the same buffer. Before curve fitting, the temperatures of dilution were subtracted

from the respective binding studies. In Origin software, the thermograms (integrated heat/injection data) collected in ITC tests were fitted using the appropriate model.

Annexin V-FITC and PI staining assay

The Thermo Fischer Scientific Annexin V-conjugated Alexa Fluor 488 apoptosis assay kit was used estimated apoptotic MCF-7 cells induced by N-1P and N-2P. After 12,24 and 48 h of being treated with ligands at the IC_{50} concentration, the cells were harvested out and washed twice with 1× PBS. Cell lysate dissolved in 1× Annexin binding buffer and stainned with Annexin-V Alexa Fluor 488 and propidium iodide (PI) for 15 min at room temperature. Then, the cells were analyzed using FACS (BD Biosciences, San Jose, CA), and the distribution of cells at different stages was found with Cell Quest 3.3 software and a statistical chart.

Western blot

MCF-7 cells were treated with N-1DEA (3.4 μM) and N-2DEA (1.3 μM) for 12 and 24 h. After the treatment at the indicated time points, the proteins were extracted from the cells using RIPA buffer (HiMedia) according to manufacturer's instruction without any modification. The protein concentration was measured using BSA protein assay kit (Takara) according to manufacturer's instruction without any modification and around 20 μg of total protein for each sample was loaded on a 15% Tris-glycine SDS-PAGE. After separation, the protein was electrotransferred onto a polyvinylidene fluoride (PVDF) membrane (Thermo Fisher Scientific). After blocking with 2.5% w/v SM powder (Himedia), the membrane was incubated with active caspase-3 antibody (catalog no. E-AB-22115; Elabscience) at a dilution of 1:1,000 at 4°C for overnight. After washing, the membrane was incubated with HRP-conjugated goat anti-mouse secondary antibody (catalog no. 626520; Thermo Fisher Scientific) at a dilution of 1:10,000 at room temperature for 1 h. After washing, ECL substrate (Takara) was added on the membrane and developed the blot onto an X-ray film. The membrane was striped further and repeated the western blot with GAPDH antibody (catalog no. MA5-35235; Invitrogen) and HRP-conjugated goat anti-rabbit secondary antibody (catalog no. 31460; Thermo Fisher Scientific) at a dilution of 1:1,000 and 1:10,000, respectively. GAPDH antibody was used as a loading control for this assay. MCF-7 cells without any treatment were used as a control.

DATA AVAILABILITY

The author confirms that the data supporting the study's conclusions are contained within the article and its supplemental information. On reasonable request, raw data supporting the findings of this study can be obtained from the corresponding author.

SUPPLEMENTAL INFORMATION

Supplemental information can be found online at https://doi.org/10.1016/j.omtn.2022.11.008.

ACKNOWLEDGMENT

The authors would like to thank the Department of Science and Technology, India, for the individual fellowship (JRF/SRF). We would also thank to the Department of Biotechnology, India, for support for project grant (BT/PR/14187/BRB/10/1413/2015). The authors would also like to thank Mr. Somok Bhowmik for his valuable suggestion in qRT-PCR and microscopic studies. A special thanks to Dr. Anuradha for constant support in the synthesis part. The authors would like to acknowledge Prof. Partha Roy and Sakshi from his lab for providing antibodies and MCF-7 cell line.

AUTHOR CONTRIBUTIONS

A.D. conceptualized the idea, and A.D. and R.B. designed the methodology. Data mining and curation and biophysical experiments were performed by A.D. Cell-based studies and RT-PCR were performed and analyzed by A.D. Synthesis of both the molecule performed by K.P. under the supervision of R.B. and M.N. The original draft was written by A.D. and was reviewed by R.B., K.P., and R.P.

DECLARATION OF INTERESTS

The authors declare no competing interests.

REFERENCES

1. Neidle, S. (2016). Quadruplex nucleic acids as novel therapeutic targets. J. Med. Chem. *59*, 5987–6011.
2. Spiegel, J., Adhikari, S., and Balasubramanian, S. (2020). The structure and function of DNA G-quadruplexes. Trends Chem. *2*, 123–136.
3. Phan, A.T., Luu, K.N., and Patel, D.J. (2006). Different loop arrangements of intramolecular human telomeric (3+1) G-quadruplexes in K+ solution. Nucleic Acids Res. *34*, 5715–5719.
4. Varshney, D., Spiegel, J., Zyner, K., Tannahill, D., and Balasubramanian, S. (2020). The regulation and functions of DNA and RNA G-quadruplexes. Nat. Rev. Mol. Cell Biol. *21*, 459–474.
5. Sen, D., and Gilbert, W. (1990). A sodium-potassium switch in the formation of four-stranded G4-DNA. Nature *344*, 410–414.
6. Clement Lin, Wu, G., Wang, K., Onel, B., Sakai, S., Shao, Y., and Yang, D. (2018). Molecular recognition of the hybrid-2 human telomeric G-quadruplex by epiberberine: insights into conversion of telomeric G-quadruplex structures. Angew. Chem. Int. Ed. Engl. *57*, 10888–10893.
7. Clark, G.R., Pytel, P.D., Squire, C.J., and Neidle, S. (2003). Structure of the first parallel DNA quadruplex-drug complex. J. Am. Chem. Soc. *125*, 4066–4067.
8. Ivancich, M., Schrank, Z., Wojdyla, L., Leviskas, B., Kuckovic, A., Sanjali, A., and Puri, N. (2017). Treating cancer by targeting telomeres and telomerase. Antioxidants *6*, E15.
9. Zehlar, A.M., Williamson, J.R., Cech, T.R., and Prescott, D.M. (1991). Inhibition of telomerase by G- quartet DNA structures. Nature *354*, 737–740.
10. Rhodes, D., and Lipps, H.J. (2015). Survey and summary G-quadruplexes and their regulatory roles in biology. Nucleic Acids Res. *43*, 8627–8637.
11. Simonsson, T., Pecinka, P., and Kubista, M. (1998). DNA tetraplex formation in the control region of c-myc. Nucleic Acids Res. *26*, 1167–1172.
12. Rankin, S., Reszka, A.P., Huppert, J., Zloh, M., Parkinson, G.N., Todd, A.K., Ladame, S., Balasubramanian, S., and Neidle, S. (2005). Putative DNA quadruplex formation within the human c-kit oncogene. J. Am. Chem. Soc. *127*, 10584–10589.
13. Dai, J., Chen, D., Jones, R.A., Hurley, L.H., and Yang, D. (2006). NMR solution structure of the major G-quadruplex structure formed in the human BCL2 promoter region. Nucleic Acids Res. *34*, 5133–5144.
14. Cogoi, S., Paramasivam, M., Filichev, V., Géci, I., Pedersen, E.B., and Xodo, L.E. (2009). Identification of a new G-quadruplex motif in the KRAS promoter and design

of pyrene-modified G4-decoys with antiproliferative activity in pancreatic cancer cells. J. Med. Chem. *52*, 564–568.

15. Sun, D., Guo, K., Rusche, J.J., and Hurley, L.H. (2005). Facilitation of a structural transition in the polypurine/polypyrimidine tract within the proximal promoter region of the human VEGF gene by the presence of potassium and G-quadruplex-interactive agents. Nucleic Acids Res. *33*, 6070–6080.

16. Qin, Y., and Hurley, L.H. (2008). Structures, folding patterns, and functions of intramolecular DNA G-quadruplexes found in eukaryotic promoter regions. Biochimie *90*, 1149–1171.

17. Yang, D., and Okamoto, K. (2010). Structural insights into G-quadruplexes: towards new anticancer drugs. Future Med. Chem. *2*, 619–646.

18. Che, T., Wang, Y.Q., Huang, Z.L., Tan, J.H., Huang, Z.S., and Chen, S.B. (2018). Natural alkaloids and heterocycles as G-quadruplex ligands and potential anticancer agents. Molecules *23*, E493.

19. Sun, D., Thompson, B., Cathers, B.E., Salazar, M., Kerwin, S.M., Trent, J.O., Jenkins, T.C., Neidle, S., and Hurley, L.H. (1997). Inhibition of human telomerase by a G-Quadruplex-Interactive compound. J. Med. Chem. *40*, 2113–2116.

20. Zagotto, G., Ricci, A., Vasquez, E., Sandoli, A., Benedetti, S., Palumbo, M., and Sissi, C. (2011). Tuning G-quadruplex vs double-stranded DNA recognition in regioisomeric lysyl-peptidyl-anthraquinone conjugates. Bioconjug. Chem. *22*, 2126–2135.

21. Pradeep, T.P., and Barthwal, R. (2016). A 4:1 stoichiometric binding and stabilization of mitoxantrone-parallel stranded G-quadruplex complex established by spectroscopy techniques. J. Photochem. Photobiol., B *162*, 106–114.

22. Kshirsagar, A.D., Panchal, P.V., Harle, U.N., Nanda, R.K., and Shaikh, H.M. (2014). Anti-inflammatory and antiarthritic activity of anthraquinone derivatives in rodents. Int. J. Inflam. *2014*, 690596.

23. Sondhi, S.M., Singh, J., Rani, R., Gupta, P.P., Agrawal, S.K., and Saxena, A.K. (2010). Synthesis, anti-inflammatory and anticancer activity evaluation of some novel acridine derivatives. Eur. J. Med. Chem. *45*, 555–563.

24. Johnson, R.K., Zee-Cheng, R.K., Lee, W.W., Acton, E.M., Henry, D.W., and Cheng, C.C. (1979). Experimental antitumor activity of aminoanthraquinones. Cancer Treat Rep. *63*, 425–439.

25. Roy, S., Ali, A., Kamra, M., Muniyappa, K., and Bhattacharya, S. (2020). Specific stabilization of promoter G-Quadruplex DNA by 2, 6-disubstituted amidoanthracene-9, 10-dione based dimeric distamycin analogues and their selective cancer cell cytotoxicity. Eur. J. Med. Chem. *195*, 112202.

26. Kawauchi, K., Urano, R., Kinoshita, N., Kuwamoto, S., Torii, T., Hashimoto, Y., Taniguchi, S., Tsuruta, M., and Miyoshi, D. (2020). Photosensitizers based on g-quadruplex ligand for cancer photodynamic therapy. Genes *11*, 1340–1413.

27. Tariq, Z., and Barthwal, R. (2019). Affinity of anticancer drug daunomycin toward Tetrahymena telomeric G-quadruplex DNA D-[GGGG(TTGGGG) 3]. ACS Omega *4*, 6347–6359.

28. Barthwal, R., and Tariq, Z. (2018). Molecular recognition of parallel g-quadruplex [d-(TTGGGGT)]4 Containing tetrahymena telomeric dna sequence by anticancer drug daunomycin: Nmr-based structure and thermal stability. Molecules *23*, E2266.

29. Pradeep, T.P., Tripathi, S., and Barthwal, R. (2016). Molecular recognition of parallel quadruplex [d-(TTGGGGT)]4 by mitoxantrone: binding with 1:4 stoichiometry leads to telomerase inhibition. RSC Adv. *6*, 71652–71661.

30. Raje, S., and Barthwal, R. (2019). Molecular recognition of 3 + 1 hybrid human telomeric G-quadruplex DNA d-[AGGG(TTAGGG)3] by anticancer drugs epirubicin and adriamycin leads to thermal stabilization. Int. J. Biol. Macromol. *139*, 1272–1287.

31. Karg, B., Funke, A., Ficht, A., Sievers-Engler, A., Lämmerhofer, M., and Weisz, K. (2015). molecular recognition and visual detection of G-quadruplexes by a dicarbocyanine dye. Chem. Eur J. *21*, 13802–13811.

32. Freyer, M.W., Buscaglia, R., Kaplan, K., Cashman, D., Hurley, L.H., and Lewis, E.A. (2007). Biophysical studies of the c-MYC NHE III1 promoter: model quadruplex interactions with a cationic porphyrin. Biophys. J. *92*, 2007–2015.

33. Manet, I., Manoli, F., Zambelli, B., Andreano, G., Masi, A., Cellai, L., and Monti, S. (2011). Affinity of the anthracycline antitumor drugs Doxorubicin and Sabarubicin for human telomeric G-quadruplex structures. Phys. Chem. Chem. Phys. *13*, 540–551.

34. Das, A., Chatterjee, S., and Suresh Kumar, G. (2017). Targeting human telomeric G-quadruplex DNA with antitumour natural alkaloid. J. Mol. Recognit. *30*, 30e2639. https://doi.org/10.1002/jmr.2639.

35. Tariq, Z., and Barthwal, R. (2018). Binding of anticancer drug daunomycin to parallel G-quadruplex DNA [d-(TTGGGGT)]4 leads to thermal stabilization: a multispectroscopic investigation. Int. J. Biol. Macromol. *120*, 1965–1974.

36. Manet, I., Manoli, F., Zambelli, B., Andreano, G., Masi, A., Cellai, L., Ottani, S., Marconi, G., and Monti, S. (2011). Complexes of the antitumoral drugs Doxorubicin and Sabarubicin with telomeric G-quadruplex in basket conformation: ground and excited state properties. Photochem. Photobiol. Sci. *10*, 1326–1337.

37. Tripathi, S., Pradeep, T.P., and Barthwal, R. (2016). Molecular recognition of parallel DNA quadruplex d(TTAGGGT)4 by mitoxantrone: binding with 1:2 stoichiometry leading to thermal stabilization and telomerase inhibition. Chembiochem *17*, 554–560.

38. Johnson, I.M., Kumar, S.G.B., and Malathi, R. (2003). De-intercalation of ethidium bromide and acridine orange by xanthine derivatives and their modulatory effect on anticancer agents: a study of dna-directed toxicity enlightened by time correlated single photon counting. J. Biomol. Struct. Dyn. *20*, 677–686.

39. Mohanty, J., Barooah, N., Dhamodharan, V., Harikrishna, S., Pradeepkumar, P.I., and Bhasikuttan, A.C. (2013). Thioflavin T as an efficient inducer and selective fluorescent sensor for the human telomeric G-quadruplex DNA. J. Am. Chem. Soc. *135*, 367–376.

40. Vorlíčková, M., Kejnovská, I., Sagi, J., Renčiuk, D., Bednářová, K., Motlová, J., and Kypr, J. (2012). Circular dichroism and guanine quadruplexes. Methods *57*, 64–75.

41. Dapić, V., Abdomerović, V., Marrington, R., Peberdy, J., Rodger, A., Trent, J.O., and Bates, P.J. (2003). Biophysical and biological properties of quadruplex oligodeoxyribonucleotides. Nucleic Acids Res. *31*, 2097–2107.

42. Li, Z., Tan, J.H., He, J.H., Long, Y., Ou, T.M., Li, D., Gu, L.Q., and Huang, Z.S. (2012). Disubstituted quinazoline derivatives as a new type of highly selective ligands for telomeric G-quadruplex DNA. Eur. J. Med. Chem. *47*, 299–311.

43. Ambrus, A., Chen, D., Dai, J., Bialis, T., Jones, R.A., and Yang, D. (2006). Human telomeric sequence forms a hybrid-type intramolecular G-quadruplex structure with mixed parallel/antiparallel strands in potassium solution. Nucleic Acids Res. *34*, 2723–2735.

44. Dai, J., Carver, M., Punchihewa, C., Jones, R.A., and Yang, D. (2007). Structure of the Hybrid-2 type intramolecular human telomeric G-quadruplex in K+ solution: insights into structure polymorphism of the human telomeric sequence. Nucleic Acids Res. *35*, 4927–4940.

45. Wang, Y., and Patel, D.J. (1993). Solution structure of the human telomeric repeat d [AG3(T2AG3)3] G-tetraplex. Structure *1*, 263–282.

46. Antonacci, C., Chaires, J.B., and Sheardy, R.D. (2007). Biophysical characterization of the human telomeric (TTAGGG)4 repeat in a potassium solution. Biochemistry *46*, 4654–4660.

47. Li, Q., Xiang, J., Li, X., Chen, L., Xu, X., Tang, Y., Zhou, Q., Li, L., Zhang, H., Sun, H., et al. (2009). Stabilizing parallel G-quadruplex DNA by a new class of ligands: two non-planar alkaloids through interaction in lateral grooves. Biochimie *91*, 811–819.

48. Agarwal, T., Roy, S., Chakraborty, T.K., and Maiti, S. (2010). Selective targeting of G-quadruplex using furan-based cyclic homooligopeptides: effect on c-MYC expression. Biochemistry *49*, 8388–8397.

49. Dai, J., Punchihewa, C., Ambrus, A., Chen, D., Jones, R.A., and Yang, D. (2007). Structure of the intramolecular human telomeric G-quadruplex in potassium solution: a novel adenine triple formation. Nucleic Acids Res. *35*, 2440–2450.

50. Bessi, I., Bazzicalupi, C., Richter, C., Jonker, H.R.A., Saxena, K., Sissi, C., Chioccioli, M., Bianco, S., Bilia, A.R., Schwalbe, H., and Gratteri, P. (2012). Spectroscopic, molecular modeling, and NMR-spectroscopic investigation of the binding mode of the natural alkaloids berberine and sanguinarine to human telomeric G-quadruplex DNA. ACS Chem. Biol. *7*, 1109–1119.

51. Shen, Z., Mulholland, K.A., Zheng, Y., and Wu, C. (2017). Binding of anticancer drug daunomycin to a TGGGGT G-quadruplex DNA probed by all-atom molecular dynamics simulations: additional pure groove binding mode and implications on designing more selective G-quadruplex ligands. J. Mol. Model. *23*, 256.

52. Kumar, P., and Barthwal, R. (2018). Structural and biophysical insight into dual site binding of the protoberberine alkaloid palmatine to parallel G-quadruplex DNA using NMR, fluorescence and Circular Dichroism spectroscopy. Biochimie *147*, 153–169.

53. Huang, H.S., Chen, I.B., Huang, K.F., Lu, W.C., Shieh, F.Y., Huang, Y.Y., Huang, F.C., and Lin, J.J. (2007). Synthesis and human telomerase inhibition of a series of regioisomeric disubstituted amidoanthraquinones. Chem. Pharm. Bull. *55*, 284–292.

54. Matsugami1, A., Yan, X.2, and Yuuki Noguchi2, H.S.M.K. (2007). Structure of a human telomeric DNA sequence stabilized by 8-bromoguanosine.pdf. FEBS J. *274*, 3545–3556.

55. Fedeles, B.I. (2017). G-quadruplex-forming promoter sequences enable transcriptional activation in response to oxidative stress. Proc. Natl. Acad. Sci. USA *114*, 2788–2790.

56. Agbandje, M., Jenkins, T.C., Mckenna, R., Reszka, A.P., and Neidle, S. (1992). Anthracene-9, 10-diones as potential anticancer agents. Synthesis, DNA-binding, and biological studies on a series of 2, 6-disubstituted derivatives. J. Med. Chem. *35*, 1418–1429.